Chapter 3

Band model of the graphene bilayer

Many of the special properties of the graphene bilayer have their origins in its lattice structure that results in the peculiar band structure that we will discuss in detail in this chapter. First we repeat the observation from Chapter 2 that the graphene bilayer in the A-B stacking[1] is just the unit cell of graphite that we depict in Fig. 3·1. Therefore, if the

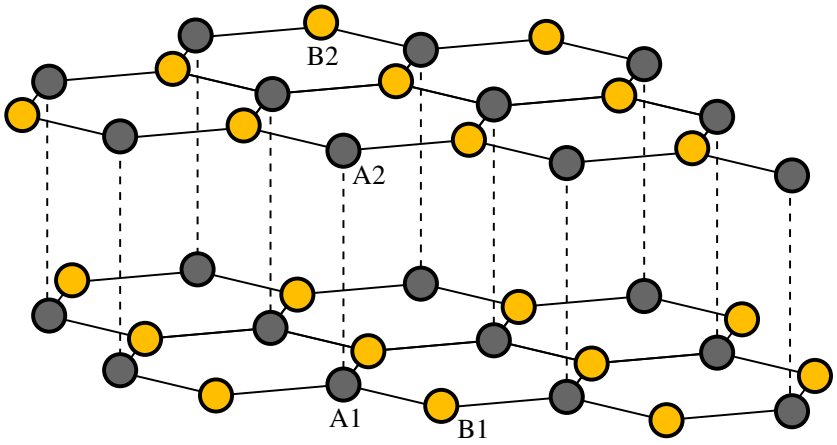

Figure 3·1: Lattice structure of the graphene bilayer. The A (B) sublattices are indicated by the darker (lighter) spheres and the planes are labeled by 1 and 2.

two planes are equivalent the symmetry analysis of graphite is also valid for the graphene bilayer. Thus we can directly use the spinor of Eq. (2.15) and the Hamiltonian in Eq. (2.17)

[1] Also known as Bernal stacking. Other stackings are also possible but the A-B stacking seems to be the most energetically favorable.

with $\Gamma = 1$ and $\gamma_2 = \gamma_5 = 0$, leading to:

$$\mathcal{H}_0(\mathbf{p}) = \begin{pmatrix} \Delta & v_{\mathrm{F}} p e^{i\phi} & t_\perp & -v_4 v_{\mathrm{F}} p e^{-i\phi} \\ v_{\mathrm{F}} p e^{-i\phi} & 0 & -v_4 v_{\mathrm{F}} p e^{-i\phi} & v_3 v_{\mathrm{F}} p e^{i\phi} \\ t_\perp & -v_4 v_{\mathrm{F}} p e^{i\phi} & \Delta & v_{\mathrm{F}} p e^{-i\phi} \\ -v_4 v_{\mathrm{F}} p e^{i\phi} & v_3 v_{\mathrm{F}} p e^{-i\phi} & v_{\mathrm{F}} p e^{i\phi} & 0 \end{pmatrix}. \tag{3.1}$$

Another way of arriving at Eq. (3.1) is to use the tight-binding model directly in the bilayer. Since the system is two-dimensional only the relative position of the atoms projected on to the x-y-plane enters into the model. The projected position of the different atoms are shown in Fig. 3·2. Since the A atoms are sitting right on top of each other in the lattice, the

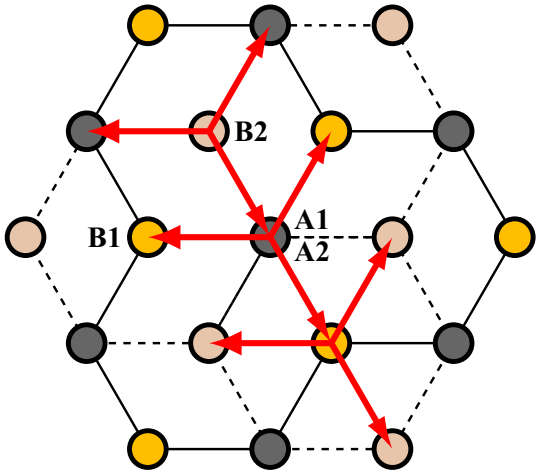

Figure 3·2: The real space lattice structure of the graphene bilayer projected onto the x-y plane showing the relative positions of the different sublattices.

hopping term between the $A1$ and $A2$ atoms are local in real space and hence a constant that we denote by $t_\perp$ in momentum space. Referring back to Section 2.1 we note that the hopping B1 $\rightarrow$ A1 [A1 $\rightarrow$ B1] gives rise to the factor $\zeta(\mathbf{k})$ [$\zeta^*(\mathbf{k})$], with $\zeta(\mathbf{k})$ defined in Eq. (2.6). Since the geometrical role of the A and B atoms are interchanged between plane 1 and plane 2 we immediately find that in Fourier space the hopping A2 $\rightarrow$ B2 [B2 $\rightarrow$ A2] gives rise to the factor $\zeta(\mathbf{k})$ [$\zeta^*(\mathbf{k})$]. Furthermore, the direction in the hopping B1 $\rightarrow$ B2

(projected on to the x-y plane) is opposite to that of hopping B1 → A1. Thus we associate a factor $v_3\zeta^*(\mathbf{k})$ to the hopping B1 → B2, where the factor $v_3 = \gamma_3/\gamma_0$ is needed because the hopping energy is γ_3 instead of $\gamma_0 = t$. Similarly, the direction of hopping B1 → A2 (projected on to the x-y plane) is the same as B1 → A1 and therefore the term $-v_4\zeta(\mathbf{k})$ goes with the hopping B1 → A2.[2] Continuing to fill in all the entries of the matrix the full tight-binding Hamiltonian in the graphene bilayer becomes:

$$\mathcal{H}_{\text{t.b.}}(\mathbf{k}) = \begin{pmatrix} \Delta & \zeta(\mathbf{k}) & t_\perp & -v_4\zeta^*(\mathbf{k}) \\ \zeta^*(\mathbf{k}) & 0 & -v_4\zeta^*(\mathbf{k}) & v_3\zeta(\mathbf{k}) \\ t_\perp & -v_4\zeta(\mathbf{k}) & \Delta & \zeta^*(\mathbf{k}) \\ -v_4\zeta(\mathbf{k}) & v_3\zeta^*(\mathbf{k}) & \zeta(\mathbf{k}) & 0 \end{pmatrix}, \tag{3.2}$$

where Δ parametrizes the difference in energy between the A and B atoms. We come back to Eq. (3.1) upon expanding this expression close to the K point. The typical behavior of the bands obtained from Eq. (3.1) is shown in Fig. 3·3. Two of the bands (labeled 3 and 4 in the figure) are moved away from the Dirac point by an energy that is given by the interplane hopping term $t_\perp$.

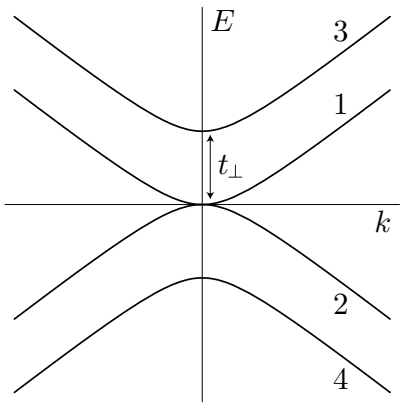

Figure 3·3: Band dispersions near the K-points in the bilayer. Bands are labeled by the numbers $1-4$ as in the text.

[2]The minus sign in front of v_4 follows from the conventional definition of γ_4 (Partoens and Peeters, 2006).

3.1 Simplified model

A simplified model that only considers the interplane hopping term between A atoms employs a matrix of the form

$$\mathcal{H}_0(\mathbf{p}) = \begin{pmatrix} 0 & v_{\mathrm{F}} p e^{i\phi(\mathbf{p})} & t_\perp & 0 \\ v_{\mathrm{F}} p e^{-i\phi(\mathbf{p})} & 0 & 0 & 0 \\ t_\perp & 0 & 0 & v_{\mathrm{F}} p e^{-i\phi(\mathbf{p})} \\ 0 & 0 & v_{\mathrm{F}} p e^{i\phi(\mathbf{p})} & 0 \end{pmatrix}. \tag{3.3}$$

From now on in this section, we use units such that $v_{\mathrm{F}} = 1$ as discussed in Section 2.1. This Hamiltonian has the advantage that it allows for relatively simple calculations. Some of the fine details of the physics might not be accurate but it will work as a minimal model and capture most of the important physics. It is important to know the qualitative nature of the terms that are neglected in this approximation, this will be discussed later in this Chapter. It is also an interesting toy model as it allows for (approximately) "chiral" particles with mass (i.e., a parabolic spectrum) at low energies as we will discuss in the next Section. For a large part of this thesis we will study the properties of the system with this simplified Hamiltonian.

3.2 Approximate effective two-band models

There are two main reasons for constructing approximate two-band models: First, on physical grounds the high-energy bands (far away from the Dirac point) should not be very important for the low-energy properties of the system. Second, it is often easier to work with 2×2 matrices instead of 4×4 matrices. In this section, we derive the low-energy effective model by doing degenerate second order perturbation theory. The quality of the expansion is good as long as $v_{\mathrm{F}} p \ll t_\perp \approx 0.35\,\mathrm{eV}$. We first present the general expression for the second-order 2×2 effective Hamiltonian, thereafter various simplified forms will be introduced. Analyses similar to the one presented here were presented in (McCann and Fal'ko, 2006) and (Nilsson et al., 2006c).

Derivation of effective models

First we decompose Eq. (3.1) into a high-energy part $\mathcal{K}_0$ and two low-energy parts $\mathcal{K}_1$ and $\mathcal{K}_2$ according to $\mathcal{H}_0 = \mathcal{K}_0 + \mathcal{K}_1 + \mathcal{K}_2$, with

$$\mathcal{K}_0 = \begin{pmatrix} \Delta & 0 & t_\perp & 0 \\ 0 & 0 & 0 & 0 \\ t_\perp & 0 & \Delta & 0 \\ 0 & 0 & 0 & 0 \end{pmatrix}, \tag{3.4}$$

$$\mathcal{K}_1 = v_{\mathrm{F}} \begin{pmatrix} 0 & pe^{i\phi} & 0 & -v_4 pe^{-i\phi} \\ pe^{-i\phi} & 0 & -v_4 pe^{-i\phi} & 0 \\ 0 & -v_4 pe^{i\phi} & 0 & pe^{-i\phi} \\ -v_4 pe^{i\phi} & 0 & pe^{i\phi} & 0 \end{pmatrix}, \tag{3.5}$$

$$\mathcal{K}_2 = v_{\mathrm{F}} \begin{pmatrix} 0 & 0 & 0 & 0 \\ 0 & 0 & 0 & v_3 pe^{i\phi} \\ 0 & 0 & 0 & 0 \\ 0 & v_3 pe^{-i\phi} & 0 & 0 \end{pmatrix}. \tag{3.6}$$

The usual manipulations (Sakurai, 1994) then given the Hamiltonian matrix in the low energy subspace as $\mathcal{K}_{\mathrm{low}} = \mathcal{K}_2 - \mathcal{K}_1^\dagger \mathcal{P}_1 (1/\mathcal{K}_0) \mathcal{P}_1 \mathcal{K}_1$, where $\mathcal{P}_1$ is the projection out of the low-energy subspace (explicitly $\mathcal{P}_1 = \mathrm{Diag}[1,\, 0,\, 1,\, 0]$). The result is:

$$\mathcal{K}_{\mathrm{low}} = \frac{v_{\mathrm{F}}^2 p^2}{t_\perp^2 - \Delta^2} \begin{pmatrix} 0 & 0 & 0 & 0 \\ 0 & 2t_\perp v_4 + \Delta(1+v_4^2) & 0 & -\big[t_\perp(1+v_4^2) + 2v_4\Delta\big] e^{-2i\phi} \\ 0 & 0 & 0 & 0 \\ 0 & -\big[t_\perp(1+v_4^2) + 2v_4\Delta\big] e^{2i\phi} & 0 & 2t_\perp v_4 + \Delta(1+v_4^2) \end{pmatrix} + \mathcal{K}_2, \tag{3.7}$$

and because this is really just a 2×2 matrix in the low-energy subspace we can write it as:

$$\mathcal{H}_{\text{eff}} = \frac{v_{\text{F}}^2 p^2}{t_\perp^2 - \Delta^2} \Big\{ \big[2t_\perp v_4 + \Delta(1+v_4^2)\big] \begin{pmatrix} 1 & 0 \\ 0 & 1 \end{pmatrix} - \big[t_\perp(1+v_4^2) + 2v_4\Delta\big] \begin{pmatrix} 0 & e^{-i2\phi} \\ e^{i2\phi} & 0 \end{pmatrix} \Big\} + v_3 v_{\text{F}} p \begin{pmatrix} 0 & e^{i\phi} \\ e^{-i\phi} & 0 \end{pmatrix}. \quad (3.8)$$

The corresponding eigenvalues are:

$$E_{\text{eff},\pm} \approx \frac{v_{\text{F}}^2 p^2}{t_\perp^2 - \Delta^2}\big[2t_\perp v_4 + \Delta(1+v_4^2)\big] \pm \sqrt{(v_3 v_{\text{F}} p)^2 + \Big\{\frac{v_{\text{F}}^2 p^2\big[t_\perp(1+v_4^2) + 2v_4\Delta\big]}{t_\perp^2 - \Delta^2}\Big\}^2 - \frac{2v_3 v_{\text{F}}^3 p^3\big[t_\perp(1+v_4^2) + 2v_4\Delta\big]}{t_\perp^2 - \Delta^2}\cos(3\phi)}. \quad (3.9)$$

This expression shows that v_4 and Δ weakly breaks the particle-hole symmetry of the system and that v_3 is responsible for breaking the cylindrical symmetry and the so-called "trigonal warping" of the energy bands. A simplified model that takes only the terms involving $t_\perp$ and the trigonal warping v_3 into account is

$$\mathcal{H}_{\text{eff}} = -\frac{v_{\text{F}}^2 p^2}{t_\perp} \begin{pmatrix} 0 & e^{-i2\phi} \\ e^{i2\phi} & 0 \end{pmatrix} + v_3 v_{\text{F}} p \begin{pmatrix} 0 & e^{i\phi} \\ e^{-i\phi} & 0 \end{pmatrix}. \quad (3.10)$$

An even simpler model which neglects both the electron-hole asymmetry and the trigonal warping is:

$$\mathcal{H}_{\text{eff}} = -\frac{v_{\text{F}}^2 p^2}{t_\perp} \begin{pmatrix} 0 & e^{-i2\phi} \\ e^{i2\phi} & 0 \end{pmatrix}. \quad (3.11)$$

This form is interesting since it gives rise to massive "chiral" quasi-particles (McCann and Fal'ko, 2006). Here "chirality" means that there exist an operator $\hat{\mathcal{C}}$ defined by

$$\hat{\mathcal{C}} \equiv -\begin{pmatrix} 0 & e^{-i2\phi} \\ e^{i2\phi} & 0 \end{pmatrix}, \quad (3.12)$$

that has the eigenvalues ± 1 and commutes with the Hamiltonian. This implies that there is another quantum number (in addition to the energy) with which one can label the states of the system.

3.3 Band structure comparisons

A comparison of the bands obtained from the simple Hamiltonian in Eq. (3.3) and those obtained from the full Hamiltonian in Eq. (3.1) on a large scale is shown in Fig. 3·4. This figure clearly shows that the gross features of the bands are correctly captured in the simple minimal model.

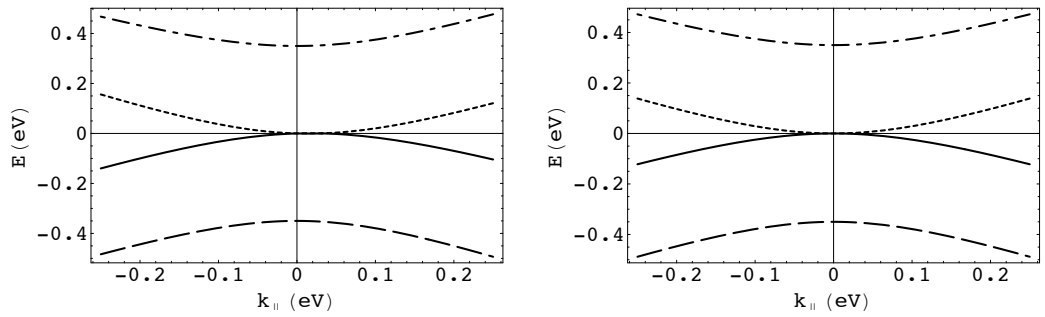

Figure 3·4: Comparison between the bands obtained from the full Hamiltonian in Eq. (3.1) and those of the simple minimal model in Eq. (3.3) along the direction $\phi = 0$ in the BZ. (a) Full Hamiltonian. (b) Minimal model Hamiltonian.

That the low-energy effective theory in Eq. (3.8) and Eq. (3.9) is accurate for low energies is shown in Fig. 3·5. But as one moves away from the Dirac point deviations from the real spectrum is clearly visible.

We show, in Figure 3·6 and in Figure 3·7, a comparison of the bands obtained from the simple minimal Hamiltonian in Eq. (3.3) and those of the full Hamiltonian in Eq. (3.1) for low energies. This shows that especially γ_3, which gives rise to the "trigonal distortion", significantly changes the behavior at the lowest energies. A normal Dirac cone is found at $\mathbf{p} = 0$ at the lowest energies, but now the Fermi-Dirac velocity is $v_3 v_{\mathrm{F}}$. There is also the

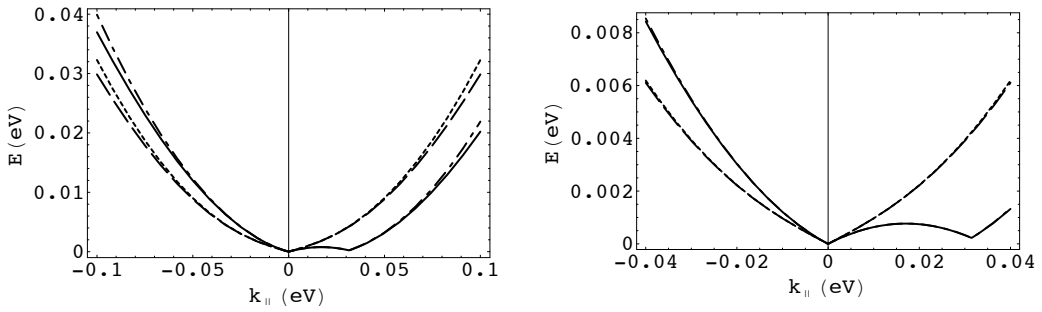

(a) (b)

Figure 3·5: Comparison between the bands obtained from the full Hamiltonian in Eq. (3.1) and those of the effective model in Eq. (3.8) along different directions in the BZ. Solid line – [$\phi = 0$, Eq. (3.1)], Dash-dotted line – [$\phi = 0$, Eq. (3.8)] , Dashed line – [$\phi = \pi/6$, Eq. (3.1)], Dotted line – [$\phi = \pi/6$, Eq. (3.8)]. (a) Larger energy scale. (b) Zoom in at low energies.

extra band crossings in the directions $\phi = 0$ and $\phi = \pm 2\pi/3$ which gives rise to elliptical Dirac cone[3] away from the point $\mathbf{p} = 0$. This structure is present at a small energy scale of the order of $\sim 1\,\text{meV}$, therefore experimental probes that are sensitive to this energy scale are necessary to be able to detect these features. Moreover, as we will see in Chapter 5, different forms of disorder can easily generate energies of this scale or larger in the real experimental samples, thus this structure might be hard to detect experimentally.

A study of few-layer graphene systems (including graphene bilayers) with plots similar to those in this chapter can be found in (Partoens and Peeters, 2006). A first-principles study with both similar scope and results also exists (Latil and Henrard, 2006).

[3]This means that there are two inequivalent perpendicular axes (1 and 2) in the cone, with two different values of the Fermi velocity $v_{\text{F}1} \neq v_{\text{F}2}$. The spectrum is then $\pm\sqrt{v_{\text{F}1}^2 p_1^2 + v_{\text{F}2}^2 p_2^2}$.

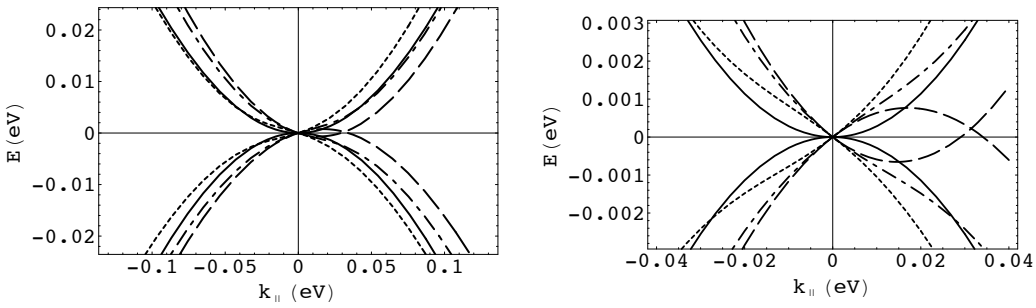

(a) (b)

Figure 3·6: Comparison between the low-energy bands obtained from the simple model in Eq. (3.3): solid lines; and those of the full Hamiltonian in Eq. (3.1) along three different directions in the BZ: $\phi = 0$ (dashed), $\phi = \pi/9$ (dashed-dotted), and $\phi = 2\pi/9$ (dotted). (a) Larger energy scale. (b) Zoom in at low energies.

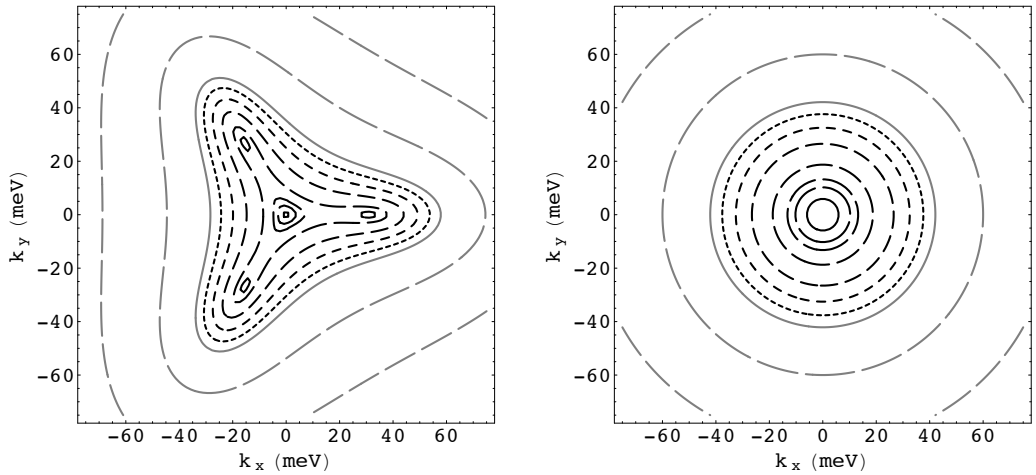

(a) (b)

Figure 3·7: Comparison between the bands obtained from the full Hamiltonian and those of the simple minimal model at low energies using a contour plot: (a) Full Hamiltonian (b) Simplified Hamiltonian. The contours are at the energies: 0.1, 0.3, 0.5, 1, 2, 3, 4 meV (black lines, ordered from the solid line to the more dotted), 5, 10, 20 meV (gray lines, same ordering).